Results in Physics 35 (2022) 105415

Contents lists available at ScienceDirect

Results in Physics

journal homepage: www.elsevier.com/locate/rinp

Optimized negative thermal expansion property in low-cost $Mg_2P_2O_7$-based bulk material

Yige Du [a], Qilong Gao [a,*], Andrea Sanson [b], Hengli Xie [a], Yangming Hu [a], Gaojie Zeng [a], Juan Guo [a], Xiao Ren [a], Erjun Liang [a,*]

[a] Key Laboratory of Materials Physics of Ministry of Education, and School of Physics and Microelectronics, Zhengzhou University, Zhengzhou 450052, China
[b] Department of Physics and Astronomy, University of Padova, Padova I-35131, Italy

ARTICLE INFO

Keywords:
Negative thermal expansion
Pyrophosphate
Phase transition
Raman

ABSTRACT

Negative thermal expansion (NTE) is an intriguing physical phenomenon, which is of great significance for the high precision application. In this work, we have realized to broaden the NTE temperature zone in $Mg_2P_2O_7$-based bulk material by doping Cu atom on the Mg site. A joint study of Raman scattering and X-ray diffraction (XRD) indicates that there are double phases in the NTE temperature zone, and the NTE of $Mg_{1.9}Cu_{0.1}P_2O_7$ bulk material comes from the phase transition of α- and β-phase. The present work provides a way to optimize negative thermal expansion property in phase transition typed materials.

Introduction

Negative thermal expansion (NTE) has been one of the hot topics in physics, chemistry and materials science since the NTE of ZrW_2O_8 in the temperature range from 0.3 to 1050 K was discovered [1–6]. The NTE phenomenon has been found in many compounds, which are driven by various mechanisms, such as low-frequency optical or acoustic phonons in framework oxides [7–15], fluorides [16,17], cyanides [18], and Prussian blue analogues [19–22]; magnetovolume effect in Mn_3AN and magnetic alloys [23–26]; spontaneous volume ferroelectrostriction in $PbTiO_3$-based compounds [27] and intermetallic charge transfer in $BiNiO_3$ [28]. In addition, giant thermal shrinkage was also reported in Mott phase transition compound Ca_2RuO_4 with oxygen vacancies [29–32].

Due to the drastic electronic structure change of the first-order phase-transition-type NTE materials, they always exhibit a sharp lattice shrinkage near the phase transition, while the temperature region is very narrow [33,34]. What's more, most of phase-transition-type NTE materials must be prepared under special process conditions, some of which are extremely difficult. For example, anti-perovskite manganese nitrides have to be sintered in a sealed quartz tube at high temperature (about 1253 K) [35], $LaCu_3Fe_4O_{12}$ is prepared at high pressure (15 GPa) and high temperature (1473 K) [36], and $PbTiO_3$ has apparent toxicity. Hence, it is important to explore new phase-transition-type NTE materials with a low-cost and easy preparation process.

Recently, several members of $A_2M_2O_7$ family compounds [37] have been found to display NTE phenomenon in a relatively wide temperature range, such as α- and β-$Cu_2V_2O_7$ [38,39], $Zn_2V_{1.7}P_{0.3}O_7$ [40], and α-$Cu_2P_2O_7$ [41]. Transverse vibrations of bridging oxygen atoms coupled with distortions of the polyhedrons seem to be responsible for the thermal contraction in these compounds. In this paper, we have studied the thermal expansion property of magnesium pyrophosphate ($Mg_2P_2O_7$). It is found that $Mg_2P_2O_7$ has quite different thermal expansion behaviors from above pyrophosphates though they have similar structure and phase transition properties. $Mg_2P_2O_7$ and its copper counterpart adopt a monoclinic structure at low temperature, and transform to high-temperature β-phase around 340 K and 350 K, respectively. $Mg_2P_2O_7$ displays a normal thermal expansion property in both α- and β-phase and exhibits a giant volume contraction (-1.73×10^{-4} K^{-1}) during the phase transition (337–351 K). It is demonstrated that the NTE window can be well shifted and broadened to cover room temperature by replacing Mg with Cu, which is conducive to a variety of applications. In contrast to the thermal shrinkage in other pyrophosphates, the giant NTE in pristine and Cu-substituted $Mg_2P_2O_7$ compounds originates from the temperature-activated phase transition instead of transverse vibrations of bridging oxygen atoms coupled with polyhedral torsional rotations. Quantitative temperature-dependent X-ray diffraction and Raman spectroscopic analyses demonstrate that the NTE in $Mg_{2-x}Cu_xP_2O_7$ compounds results from the mass fractional changes of the α- and β- phase during phase transition.

* Corresponding authors.
E-mail addresses: qilonggao@zzu.edu.cn (Q. Gao), ejliang@zzu.edu.cn (E. Liang).

https://doi.org/10.1016/j.rinp.2022.105415
Received 11 January 2022; Received in revised form 25 February 2022; Accepted 9 March 2022
Available online 11 March 2022

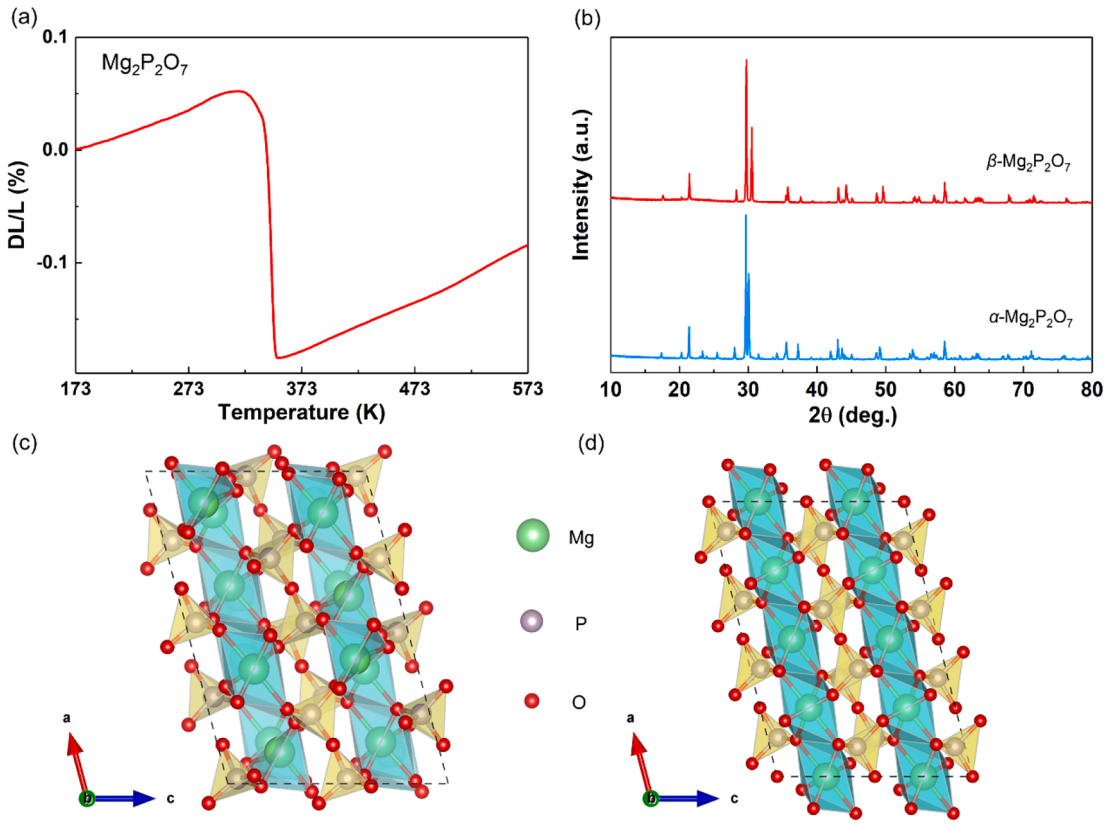

Fig. 1. (a) The temperature dependence of linear thermal expansion of $Mg_2P_2O_7$. (b) The powder XRD patterns for α-$Mg_2P_2O_7$ at room temperature and β-$Mg_2P_2O_7$ at 473 K. (c) Crystal structure of α-$Mg_2P_2O_7$ (space group $B2_1/c$). (d) Crystal structure of β-$Mg_2P_2O_7$ (space group C_2/m).

Experiment

$Mg_{2-x}Cu_xP_2O_7$ (x = 0, 0.05, 0.1, 0.2) were synthesized by high temperature solid-state reactions. MgO (analytical pure, 99.99%, Aladdin), CuO (99%, Aladdin), and $NH_4H_2PO_4$ (99%, Aladdin) were weighed and mixed evenly. The mixtures were pressed into pellets in a 769YP-15A tablet press under 2 MPa for 3 min. The cylindrical samples were sintered in a box-type furnace, and heated at a rate of 5 K/min. Pre-sintering was held at 1423 K for 1 h and then cooled to room temperature. Subsequently, the powders were again pressed and sintered for 5 h at 1423 K, followed by nature cooling to room temperature.

X-ray diffractometer (SmartLab, Japan, Cu, Kα) was used to collect the diffraction patterns of samples from 80 to 573 K. The crystal structures were obtained by the refinement of XRD patterns via the Rietveld analysis. The macroscopic linear thermal expansion of samples were measured by the LINSEIS DIL L76 thermal dilatometer (LINSEIS, Germany) with a rising and cooling rate of 5 K/min. A Raman spectrometer (HORIBA, France, 532 nm) was used to collect the Raman spectra of samples from 100 to 473 K.

Results and discussion

Giant NTE accompanied by the structure transition in $Mg_2P_2O_7$

The linear thermal expansion curve of $Mg_2P_2O_7$ measured by the thermal dilatometer is shown in Fig. 1a. The relative length of bulk $Mg_2P_2O_7$ increases with the increase of temperature below 313 K and above 351 K, but it shrinks abruptly from 337 to 351 K (α_l = -1.73 × 10^{-4} K^{-1}). The sudden change in volume indicates a first-order phase transition in this region. The XRD patterns of $Mg_2P_2O_7$ measured at room temperature and 473 K confirm the phase transition from low-temperature α-$Mg_2P_2O_7$ to high-temperature β-$Mg_2P_2O_7$ (Fig. 1b). Although colossal volume shrinkage has also been reported in $BiNiO_3$ [28] and $LaCu_3Fe_4O_{12}$ [42] during phase transition by temperature-induced intermetallic charge transfer, $Mg_2P_2O_7$ has an obvious advantage in atmospheric pressure preparation.

The crystal structures of α- and β-$Mg_2P_2O_7$ are shown in Fig. 1(c, d). In α-phase (space group $B2_1/c$, a = 13.198 Å, b = 8.295 Å, c = 9.072 Å, β = 104.9°, Z = 8), there are two kinds of atom positions of Mg and P atoms and seven for O atoms. Each MgO_5/MgO_6 polyhedron (blue) is connected by double O atoms. The two PO_4 tetrahedrons are connected to form a P_2O_7 group, which is alternately associated with the center of symmetry or the double helix axis. The P-O-P bond angle is bent to 144°. The cationic polyhedron and the P_2O_7 anion group are connected by O atoms. Once the sample transforms into the β-phase (space group C_2/m, a = 6.494 Å, b = 8.28 Å, c = 4.522 Å, β = 103.8°, Z = 2), the central bond angle will become linear [43]. Each MgO_6 irregular octahedron is connected by double O atoms. There is one O atom at the corner, and the central O atom in the P_2O_7 group oscillates laterally to convert the P-O-P bond angle to 180°. These groups form a sheet that is parallel to the *ab* plane, in which the ions are located approximately double-thirds of the way through the octahedral pores of the closely spaced oxygen atoms. Each O atom in these sheets is bound to double cations. Linear P-O-P groups are located between these lamellae opposite the empty octahedral positions. The symmetry of $Mg_2P_2O_7$ in the β-phase is significantly higher and all the three equivalent axes are smaller than in the α-phase, particularly, the *a*-axis and *c*-axis contract sharply after the phase transition, contributing to the giant NTE on a macroscopic scale.

Tuning the phase transition temperature and the NTE window

The volume contraction of $Mg_2P_2O_7$ is huge but only occurs within a rather narrow temperature window, similar to the cases induced by the magnetovolume effect and charge transfer. Tuning the phase transition

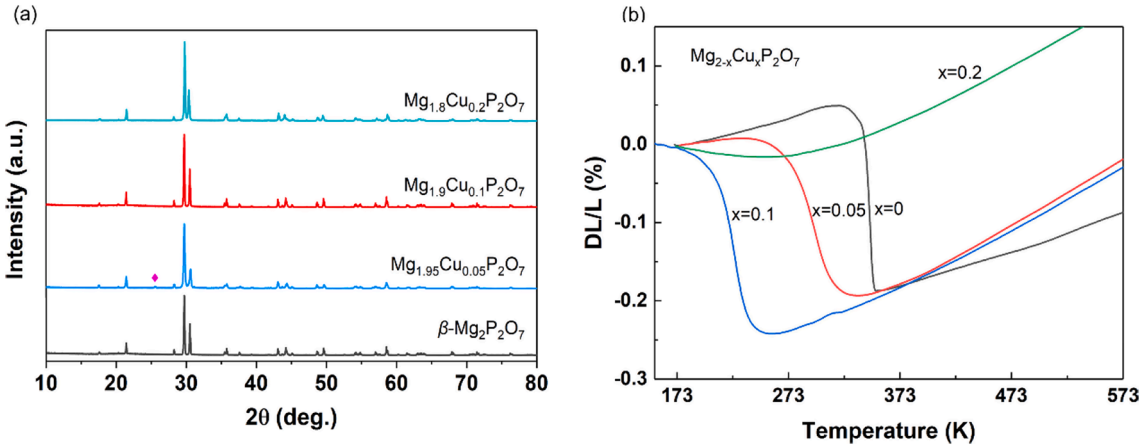

Fig. 2. (a) The room temperature XRD patterns for $Mg_{2-x}Cu_xP_2O_7$ (x = 0.05, 0.1, and 0.2) and β-$Mg_2P_2O_7$. (b) The temperature dependence of linear thermal expansion of $Mg_{2-x}Cu_xP_2O_7$ (x = 0, 0.05, 0.1, 0.2).

Table 1
The NTE behaviors of $Mg_{2-x}Cu_xP_2O_7$ (x = 0, 0.05, 0.1, and 0.2).

$Mg_{2-x}Cu_xP_2O_7$	α_l (10^{-6} K^{-1})	T_s (K)	T_f (K)	ΔT (K)
x = 0	−57.6	337	351	14
x = 0.05	−27.2	243	333	90
x = 0.1	−28.4	160	260	100
x = 0.2	−0.57	173	300	127

temperature and broadening the NTE window are of significance for a variety of applications. Taking the factor of ionic radius and electronegativity, we adopt the Cu atom to replace the Mg atom. We also noted that $Cu_2P_2O_7$ has a much larger NTE temperature zone [41]. Fig. 2a shows the XRD patterns of $Mg_{2-x}Cu_xP_2O_7$ (x = 0.05, 0.1, and 0.2) at room temperature. It can be seen that the diffraction pattern of $Mg_{1.95}Cu_{0.05}P_2O_7$ can not only be indexed by the β-$Mg_2P_2O_7$, but also contain a characteristic peak of α-$Mg_2P_2O_7$, which is marked by the purple diamond. However, the $Mg_{1.9}Cu_{0.1}P_2O_7$ and $Mg_{1.8}Cu_{0.2}P_2O_7$ convert completely into the β-phase. The Fig. 2b shows the linear thermal expansion of $Mg_{2-x}Cu_xP_2O_7$ (x = 0, 0.05, 0.1, and 0.2) samples. With the continuous increase of the doping Cu atom, the NTE temperature region of the $Mg_{2-x}Cu_xP_2O_7$ sample gradually moves to the low-temperature region (Table 1). $Mg_2P_2O_7$ shows NTE with a temperature region of 14 K around the phase transition point. When the substitution amount of Cu is 0.05, the linear coefficient of thermal expansion (CTE) is -27.2×10^{-6} K^{-1} between 243 and 333 K. With the substitution of Cu up to 0.1, the linear CTE is -28.4×10^{-6} K^{-1} between 160 and 260 K, whose NTE temperature window increase to 100 K. Intriguingly, a zero thermal expansion (ZTE) has been obtained between 173 and 300 K in $Mg_{1.8}Cu_{0.2}P_2O_7$. The NTE temperature region of the series samples all occur near the phase transition point. The addition of Cu reduces the phase transition temperature point of $Mg_2P_2O_7$ and mitigates the phase transition process.

The V element is also used to regulate the thermal expansion of $Mg_2P_{2-x}V_xO_7$ (x = 0, 0.05, and 0.1). As shown in Fig. 3a, the $Mg_2P_{1.95}V_{0.05}O_7$ has a similar diffraction pattern as the α-$Mg_2P_2O_7$, while α-$Mg_2P_2O_7$ cannot be observed in $Mg_2P_{1.9}V_{0.1}O_7$. Unlike $Mg_{2-x}Cu_xP_2O_7$, the addition of the V atom only regulated the phase transition points, but the broadening effect on the NTE temperature region is not obvious (Fig. 3b and Table 2). Therefore, the $Mg_{1.9}Cu_{0.1}P_2O_7$, due to the larger NTE temperature window and suitable NTE magnitude, has been selected to further study the NTE mechanism.

Phase analysis by temperature-dependent XRD

In order to reveal the NTE mechanism of $Mg_{1.9}Cu_{0.1}P_2O_7$, we need to extract detailed structural information from the temperature

Table 2
The NTE behaviors of $Mg_2P_{2-x}V_xO_7$ (x = 0, 0.05, and 0.1).

$Mg_2P_{2-x}V_xO_7$	α_l (10^{-6} K^{-1})	T_s (K)	T_f (K)	ΔT (K)
x = 0	−57.6	337	351	14
x = 0.05	−78.9	315	343	28
x = 0.1	−127.5	282	313	31

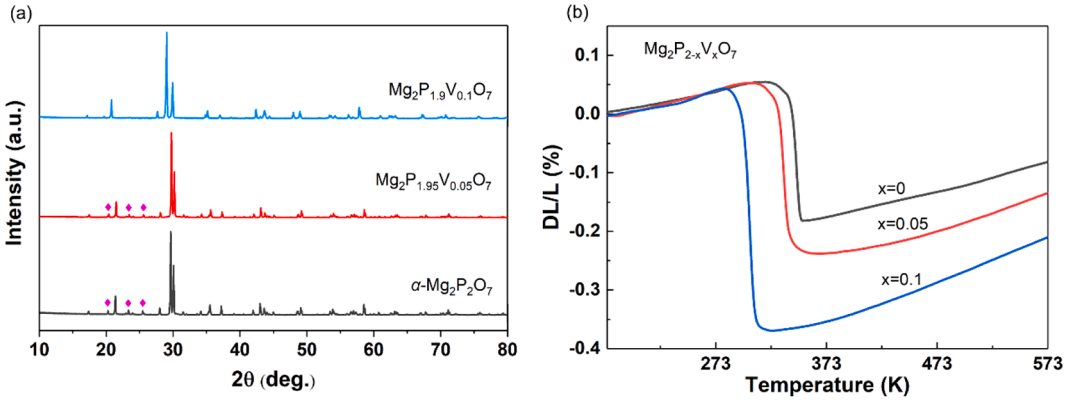

Fig. 3. (a) The room temperature powder XRD patterns for $Mg_2P_{2-x}V_xO_7$ (x = 0, 0.05, and 0.1). (b) The temperature dependence of linear thermal expansions of $Mg_2P_{2-x}V_xO_7$ (x = 0, 0.05, and 0.1).

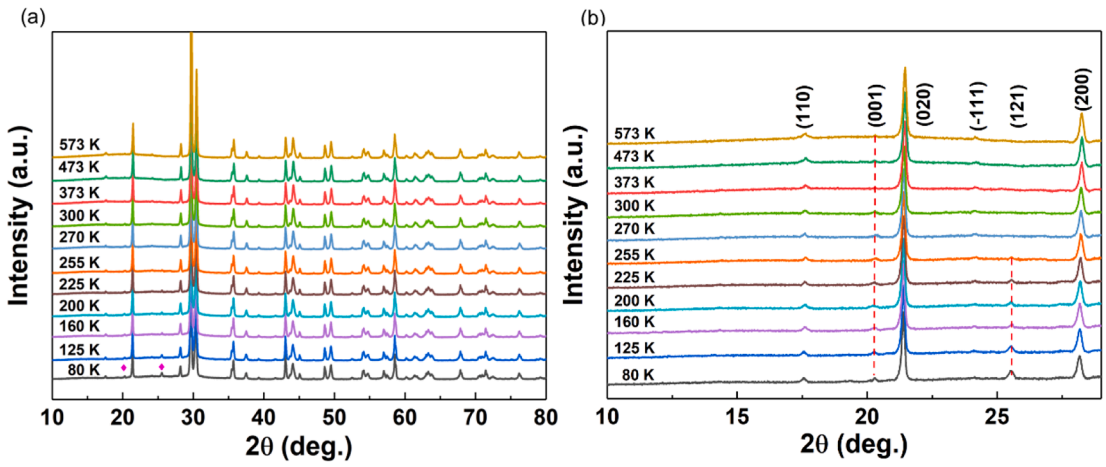

Fig. 4. (a) Temperature-dependent XRD patterns of $Mg_{1.9}Cu_{0.1}P_2O_7$. (b) Amplification of low-angle diffraction patterns.

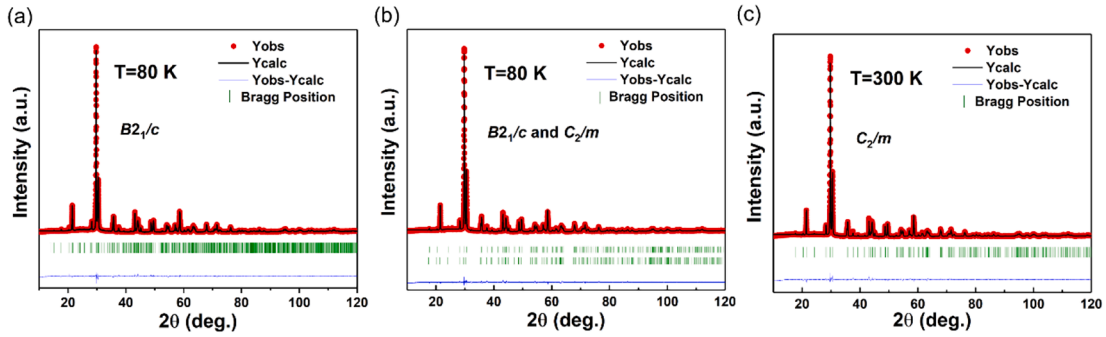

Fig. 5. Full-profile refinement of XRD patterns of $Mg_{1.9}Cu_{0.1}P_2O_7$ at 80 K by (a) single-phase and (b) double-phase model. (c) Full-profile refinement of XRD patterns of $Mg_{1.9}Cu_{0.1}P_2O_7$ at 300 K by single-phase model.

dependence of XRD data. Fig. 4a shows the temperature-dependent XRD patterns of $Mg_{1.9}Cu_{0.1}P_2O_7$ between 80 and 573 K and the low-angle patterns are shown in Fig. 4b to clearly observe the phase change. It can be seen that the intensity of (0 0 1) diffraction peak decreases as the temperature rises. The intensity of the α-phase (1 2 1) characteristic diffraction peak weakens slightly between 80 and 160 K, but decreases significantly above 160 K until it disappeared completely at 270 K. It indicated that the rate of transition from α- to β-phase is accelerated above 160 K until the phase transition is completed at 270 K, that is, the sample is fully converted to β-phase above 270 K. Hence, the XRD patterns above 270 K can be well refined with the space group C_2/m, while the patterns between 160 and 270 K should be refined by double-phase structure model.

Here, we have adopted two structural models of the single-phase (space group $B2_1/c$) and double-phase to fit the diffraction patterns below 270 K. Fig. 5(a, b) display the results of single-phase (space group $B2_1/c$) and double-phase refinement at 80 K, respectively. The reliability factors obtained by single-phase refinement are as follows: $R_p = 11.7$, $R_{exp} = 6.84$, and $\chi^2 = 2.68$. By contrast, the results obtained by double-phase refinement are more reliable ($R_p = 10.7$, $R_{exp} = 6.68$, and $\chi^2 = 2.41$). Therefore, the $Mg_{1.9}Cu_{0.1}P_2O_7$ is mainly α-phase and also contains a small amount of β-phase below 270 K. Fig. 6c shows the XRD patterns at 300 K, which can be well refined by the space group C_2/m ($R_p = 10.3$, $R_{exp} = 6.42$, $\chi^2 = 2.55$). It should be noted that the NTE phenomenon in $Mg_{1.9}Cu_{0.1}P_2O_7$ is caused by the coexistence of the double phase and this phenomenon is not isolated, since recent studies have observed the same phenomenon in $Zn_{1.6}Mg_{0.4}P_2O_7$ [44], but also in some magnetic materials such as Mn_3ZnN [45]and $Hf_{0.6}Ti_{0.4}Fe_2$ [46].

In order to investigate the relationship of NTE and phase transition, the phase proportion of $Mg_{1.9}Cu_{0.1}P_2O_7$ as a function of temperature has been extracted. Fig. 6a shows the unit cell volumes of $Mg_{1.9}Cu_{0.1}P_2O_7$ as a function of temperature (the double-phase model for 80–255 K and the single-phase model for 270–573 K). The results indicated that the unit cell volumes of the α-phase is much larger than that of β-phase, and both the α- and β-phase displays positive thermal expansion (PTE) behavior. However, the macroscopic linear thermal expansion of $Mg_{1.9}Cu_{0.1}P_2O_7$ decreased with increasing temperature (160–260 K). To explain this abnormal phenomenon, we have extracted the temperature dependent mass fraction of α- and β-phase from the structure refinement (Fig. 6b). Below 270 K, the mass fraction of the α-phase decreased with the increase of temperature, while the mass fraction of the β-phase is opposite. It should be noted that the phase transition rate of the sample below 160 K is much slower than that between 160 K and 255 K, which clearly indicates that the NTE has a direct relationship with the phase transition rate. The concept of the average unit cell volumes has been used to analyze this effect, which is based on unit cell volumes and phase proportion of the double phase (Fig. 6c). Here, the $V_{average} = 1/4V_\alpha H_\alpha + V_\beta H_\beta$, where the $V_{average}$ represents the average unit cell volume, V_α and V_β stand for the unit cell volumes of α- and β-phase, respectively, H_α and H_β are the mass fraction of the correlative phase, the constant 1/4 means that the volume of α-phase is four times that of β-phase. It is interesting to find that the average unit cell volumes show NTE phenomenon in the temperature range of 160–255 K, and the CTE is $\alpha_V = -26.06 \times 10^{-6}$ K^{-1}. One could observe that most of the samples switch from the large volume α-phase to the small volume β-phase between 160 and 255 K, resulting in a drastic contraction of the sample volume, which exhibits NTE behavior. Thus, $Mg_{1.9}Cu_{0.1}P_2O_7$ exhibits NTE property only between 160 and 255 K. Not coincidentally, the same NTE properties were

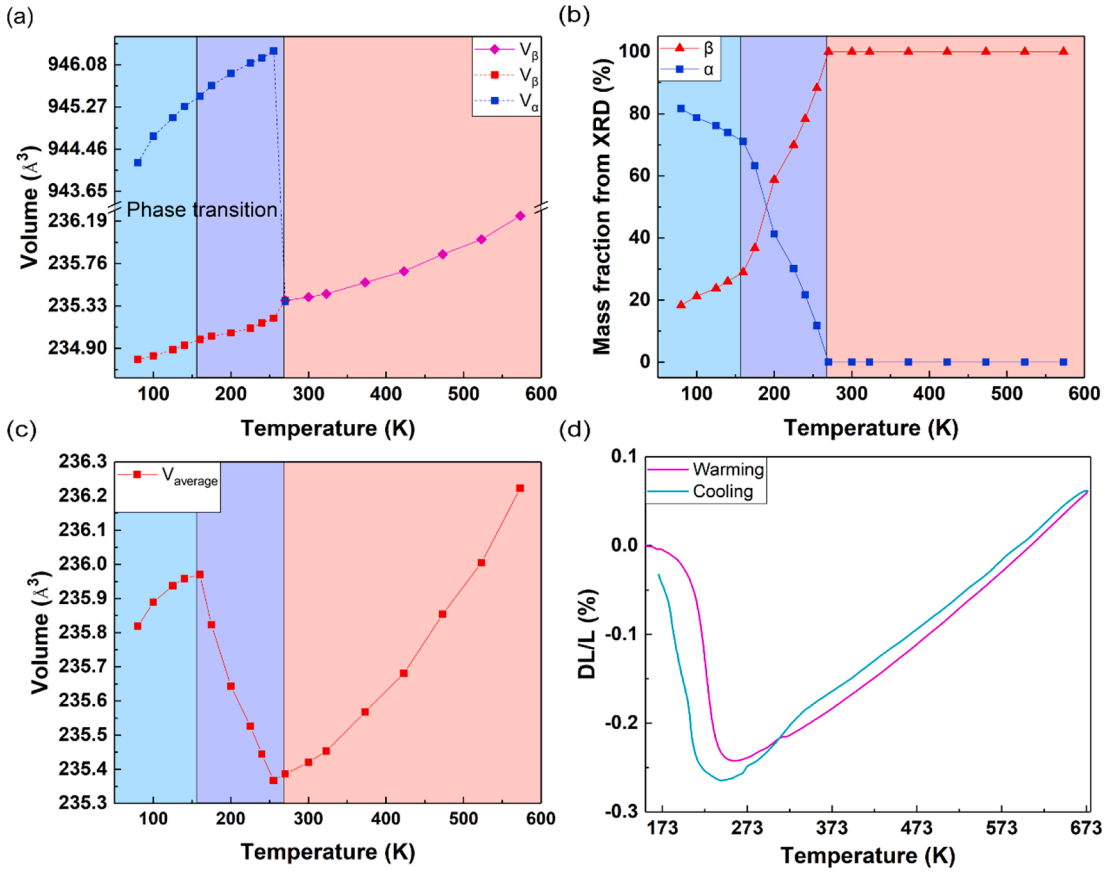

Fig. 6. Temperature dependence of (a) unit cell volumes and (b) the mass fractions of α- and β-phases. (c) Average unit cell volumes as a function of temperature. (d) Cyclic measurements of $Mg_{1.9}Cu_{0.1}P_2O_7$ by the thermal dilatometer.

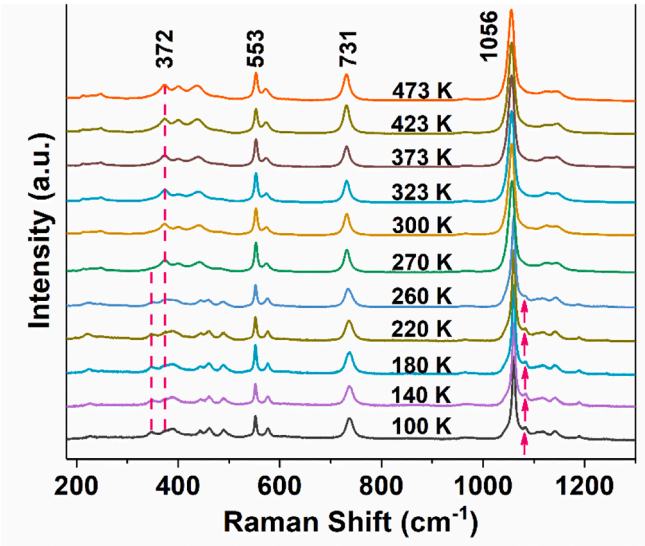

Fig. 7. Raman spectra of $Mg_{1.9}Cu_{0.1}P_2O_7$ at different temperatures.

found in $Zn_{2-x}Mg_xP_2O_7$ in a recent work of Takenaka and co-workers [44]. The volume thermal expansion of $Zn_{1.6}Mg_{0.4}P_2O_7$ was analyzed by synchrotron x-ray diffraction in the temperature 100–500 K, and it was found a huge volume contraction at 280–350 K. The crystallographic analysis revealed that the low-temperature α-phase and the high-temperature β-phase coexist in the NTE temperature region, and the fraction of larger volume α-phase decreases gradually with the temperature increases [44]. These findings are consistent with our results. Fig. 6d shows a cycle thermal expansion curve of $Mg_{1.9}Cu_{0.1}P_2O_7$, which suggests that the macroscopic NTE of the sample is repeatable. It should also be noted that the change trend of average unit cell volume obtained by the refinement of the temperature-dependent XRD is consistent with the macroscopic NTE characteristic measured with the thermal dilatometer.

Raman spectrum

The phase transition process of the sample can also be confirmed by the Raman spectroscopy (Fig. 7). The Raman peaks of different wavenumbers represent different vibration modes: the Raman peaks between 300 and 500 cm^{-1} represent the bending vibration mode of the bridge P-O-P; the Raman peaks between 500 and 600 cm^{-1} correspond to the bending vibration mode of $[PO_4]^{3-}$ element [47]. Symmetric stretching of the $[P_2O_7]^{4-}$ bridge P-O-P can be observed around approximately 680–800 cm^{-1}, and antisymmetric stretching vibration of the $[P_2O_7]^{4-}$ bridge P-O-P can be observed at 930–970 cm^{-1}; the strong vibration modes of 1000–1200 cm^{-1} are contributed by the stretching vibration of PO_4^{3-}. In addition, there are deformation and torsion modes of PO_4 polyhedron and bridge P-O-P in 200–430 cm^{-1} [48]. Temperature dependence of Raman spectra could clearly show the phase transition process of the samples. It can be seen that the intensity of the peak at 1080 cm^{-1} decreases with increasing temperature between 100 and 260 K, and disappears completely above 260 K. It means that the phase transition has been completed and the sample is completely transformed into β-phase above 260 K [49], which is consistent with the results measured by temperature-dependent XRD.

It has been reported that $Mg_2P_2O_7$ exists the coexistence of α-phase

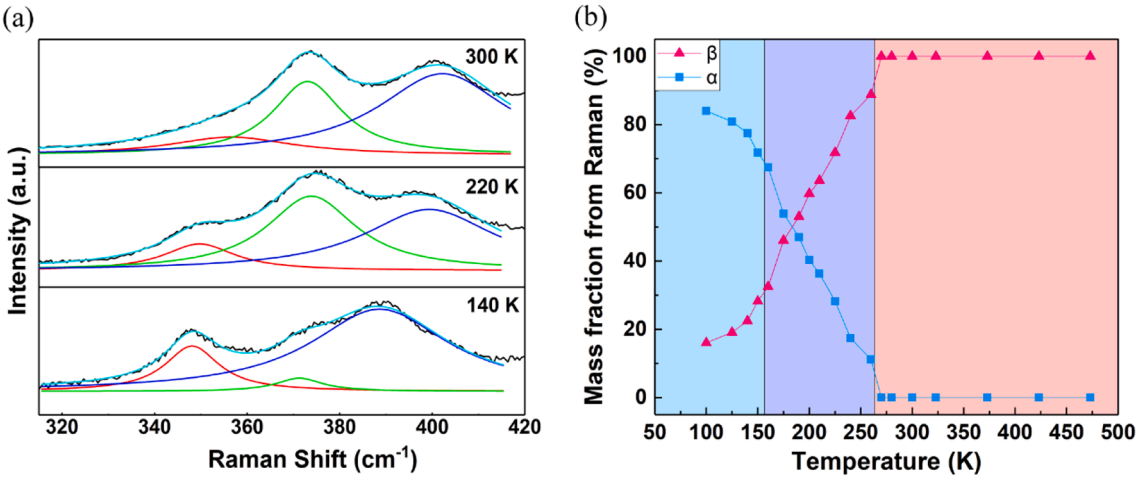

Fig. 8. (a) Amplification of the fitting results of the Raman peak intensity at 348 $cm^{-1}$and 372 cm^{-1}. (b) Temperature dependence of mass fractions of α- and β-phase extracted from Raman.

and β-phase in the phase transition process [43]. However, the phase transition process of $Mg_2P_2O_7$ is relatively quick and the NTE temperature region is really narrow, so it is not easy to observe the coexistence of the double phases. Once copper atoms are doped, the phase transition process slows down, and the NTE temperature region is broadened. The transformation from α- to β-phase can be characterized by the deformation of several Raman peaks on the Raman spectrum. As shown in Fig. 8a, the red fitted lines represent the peak at 348 cm^{-1} and the green fitted lines represent the peak at 372 cm^{-1}. The peak intensity of 348 cm^{-1} decreases with increasing temperature, while the peak intensity of 372 cm^{-1} is getting stronger, corresponding to the mass fraction of double-phase transition. We have performed Lorentz fitting for the peak intensity of 348 cm^{-1} and 372 cm^{-1}, using the peak of 553 cm^{-1} as the internal standard. The function of the intensity ratio of the double peaks with the change of temperature have been obtained, and the relative mass fractions of α-phase and β-phase in the phase transformation process have been obtained from the quantitative analysis of the Raman spectrum. As shown in Fig. 8b, the content of the α-phase decreases with the increase of temperature, while the content of the β-phase is on the contrary. The transition rate from α- to β-phase is relatively moderate between 100 and 160 K, and significantly accelerates between 160 and 260 K, until the sample completely converts to β-phase above 260 K. This result is consistent with the change function of double-phase proportion obtained by XRD.

Conclusion

In summary, we have successfully broadened NTE temperature zone in $Mg_2P_2O_7$-based materials through the doping of Cu. The NTE temperature zone of $Mg_{2-x}Cu_xP_2O_7$ can be broadened from 14 K ($Mg_2P_2O_7$) to 100 K ($Mg_{1.9}Cu_{0.1}P_2O_7$). The results of temperature-dependent XRD indicates that the NTE of $Mg_{1.9}Cu_{0.1}P_2O_7$ is caused by the change of proportion of α- and β-phase. The role of the Cu atom mitigates the transition rate from α- to β-phase and prolongs the temperature range of two-phase coexistence, which broadens the NTE temperature zones. Such phenomenon has been also observed by temperature-dependent Raman scattering, which is confirmed by the fitting results of the characteristic peaks. This work provides some insights to optimize the NTE property in most phase transition materials.

Declaration of Competing Interest

The authors declare that they have no known competing financial interests or personal relationships that could have appeared to influence the work reported in this paper.

Acknowledgements

This work was supported by the National Natural Science Foundation of China (Grant Nos. 11874328, 22071221, 21905252, 12004339), Natural Science Foundation of Henan Province (No. 212300410086), and China Postdoctoral Science Foundation (No. 2018M640679 and 2019T120629).

Author statement

Q.L. Gao and E.J. Liang conceived the idea and designed the experiments. Y. Du prepared the samples and performed the measurements. Y. Hu, G. Zeng and J. Guo analyzed and discussed the data of the X-ray diffraction. H. Xie and X. Ren assisted in the Raman experiments. All authors contributed to the discussions and revision. Y. Du, Q.L. Gao and E.J. Liang wrote the manuscript with help for the revision from all coauthors.

References

[1] Mary TA, Evans JSO, Vogt T, Sleight AW. Negative thermal expansion from 0.3 to 1050 kelvin in ZrW_2O_8. Science 1996;272(5258):90–2. https://doi.org/10.1126/science.272.5258.90.
[2] Chen J, Hu L, Deng JX, Xing XR. Negative thermal expansion in functional materials: controllable thermal expansion by chemical modifications. Chem Soc Rev 2015;44(11):3522–67. https://doi.org/10.1039/c4cs00461b.
[3] Dove MT, Fang H. Negative thermal expansion and associated anomalous physical properties: review of the lattice dynamics theoretical foundation. Rep Prog Phys 2016;79(6):066503. https://doi.org/10.1088/0034-4885/79/6/066503.
[4] Liang EJ, Sun Q, Yuan HL, Wang JQ, Zeng GJ, Gao QL. Negative thermal expansion: mechanisms and materials. Front Phys 2021;16(5):53302. https://doi.org/10.1007/s11467-021-1070-0.
[5] Sanson A. EXAFS spectroscopy: a powerful tool for the study of local vibrational dynamics. Microstructures 2021;1(1):2021004. https://doi.org/10.20517/microstructures.2021.03.
[6] Mittal R, Gupta MK, Chaplot SL. Phonons and anomalous thermal expansion behaviour in crystalline. Solids Prog Mater Sci 2018;92:360–445. https://doi.org/10.1016/j.pmatsci.2017.10.002.
[7] Katayama N, Otsuka AK, Mitamura M, Yokoyama Y, Okamoto Y, Takenaka K. Microstructural effects on negative thermal expansion extending over a wide temperature range in β-$Cu_{1.8}Zn_{0.2}V_2O_7$. Appl Phys Lett 2018;113(18):181902. https://doi.org/10.1063/1.5055304.
[8] Salke NP, Gupta MK, Rao R, Mittal R, Deng JX, Xing XR. Raman and ab initio investigation of negative thermal expansion material $TaVO_5$: insights into phase stability and anharmonicity. J Appl Phys 2015;117(23):235902. https://doi.org/10.1063/1.4922744.
[9] Shi NK, Sanson A, Venier A, Fan LL, Sun CJ, Xing XR, et al. Negative and zero thermal expansion in α-$Cu_{2-x}Zn_xV_2O_7$ solid solutions. Chem Commun 2020;56(73):10666–9. https://doi.org/10.1039/d0cc04505e.

[10] Yuan HL, Wang CY, Gao QL, Zeng GJ, Guo J, Chao MJ, et al. A linear scaling law for predicting phase transition temperature via averaged effective electronegativity derived from $A_2M_3O_{12}$-based compounds. Mater Horiz 2021;8(9):2562–8. https://doi.org/10.1039/d1mh00812a.

[11] Liu HF, Sun WK, Zhang ZP, Lovings L, Lind C. Thermal expansion behavior in the $A_2M_3O_{12}$ family of materials. Solids 2021;2(1):87–107. https://doi.org/10.3390/solids2010005.

[12] Zeng GJ, Yuan HL, Guo J, Sun Q, Gao QL, Chao MJ, et al. Hydrate formation and its effects on the thermal expansion properties of $HfMgW_3O_{12}$. Phys Chem Chem Phys 2020;22(22):12605–12. https://doi.org/10.1039/d0cp01446j.

[13] Luo Y, Qiao YQ, Gao QL, Wang JQ, Guo J, Ren X, et al. Anomalous thermal expansion in Ta_2WO_8 oxide semiconductor over a wide temperature range. Inorg Chem 2021;60(23):17758–64. https://doi.org/10.1021/acs.inorgchem.1c02377.

[14] Wei W, Gao QL, Guo J, Chao MJ, He LH, Chen J, et al. Realizing isotropic negative thermal expansion covering room temperature by breaking the superstructure of ZrV_2O_7. Appl Phys Lett 2020;116(18):181902. https://doi.org/10.1063/1.5143691.

[15] Wang JQ, Xu P, Yuan HL, Gao QL, Sun Q, Liang EJ. Negative thermal expansion driven by acoustic phonon modes in rhombohedral Zn_2GeO_4. Results Phys 2020;19:103531. https://doi.org/10.1016/j.rinp.2020.103531.

[16] Greve BK, Martin KL, Lee PL, Chupas PJ, Chapman KW, Wilkinson AP. Negative thermal expansion from a simple structure: cubic ScF_3. J Am Chem Soc 2010;132(44):15496–8. https://doi.org/10.1021/ja106711v.

[17] Hu L, Chen J, Xu JL, Wang N, Han F, Ren Y, et al. Atomic linkage flexibility tuned isotropic negative, zero, and positive thermal expansion in $MZrF_6$ (M = Ca, Mn, Fe Co, Ni, and Zn). J Am Chem Soc 2016;138(44):14530–3. https://doi.org/10.1021/jacs.6b08746.

[18] Ding P, Liang EJ, Jia Y, Du ZY. Electronic structure, bonding and phonon modes in the negative thermal expansion materials of $Cd(CN)_2$ and $Zn(CN)_2$. J Phys-Condensed Matter 2008;20(27):275224. https://doi.org/10.1088/0953-8984/20/27/275224.

[19] Gao QL, Wang JQ, Sanson A, Sun Q, Liang EJ, Xing XR, et al. Negative thermal expansion in framework compound $AgB(CN)_4$ via the concept of average atomic volume. J Am Chem Soc 2020;142(15):6935–9. https://doi.org/10.1021/jacs.0c02188.

[20] Gao QL, Sun Y, Shi NK, Milazzo R, Pollastri S, Olivi L, et al. Large isotropic negative thermal expansion in water-free Prussian blue analogues of $ScCo(CN)_6$. Scr Mater 2020;187:119–24. https://doi.org/10.1016/j.scriptamat.2020.05.041.

[21] Gao QL, Liang EJ, Xing XR, Chen J. Negative thermal expansion in Prussian blue analogues. Chem J Chin Univ 2020;41(3):388–400. https://doi.org/10.7503/cjcu20190631.

[22] Gao QL, Sun Q, Venier A, Sanson A, Huang QZ, Jia Y, et al. The role of average atomic volume in predicting negative thermal expansion: the role of *RE*$Fe(CN)_6$. Sci China Mater 2022;65(2):553–7. https://doi.org/10.1007/s40843-021-1797-3.

[23] Sun ZH, Song XY, Yin FX, Sun LX, Yuan XK, Liu XM. Giant negative thermal expansion in ultrafine-grained $Mn_3(Cu_{1-x}Ge_x)N$ (x=0.5) bulk. J Phys D Appl Phys 2009;42(12):122004. https://doi.org/10.1088/0022-3727/42/12/122004.

[24] Takenaka K, Takagi H. Giant negative thermal expansion in Ge-doped anti-perovskite manganese nitrides. Appl Phys Lett 2005;87(26):261902. https://doi.org/10.1063/1.2147726.

[25] Zhu F, Lin JC, Jiang WB, Yang C, Li LF, Zhang XK, et al. Enhanced mechanical properties and large magnetocaloric effect in epoxy-bonded $Mn_{0.98}CoGe$. Scr Mater 2018;150:96–100. https://doi.org/10.1016/j.scriptamat.2018.02.044.

[26] Song YZ, Shi NK, Deng SQ, Xing XR, Chen J. Negative thermal expansion in magnetic materials. Prog Mater Sci 2021;121:100835. https://doi.org/10.1016/j.pmatsci.2021.100835.

[27] Chen J, Wang FF, Huang QZ, Hu L, Song XP, Deng JX, et al. Effectively control negative thermal expansion of single-phase ferroelectrics of $PbTiO_3$-(Bi, La)FeO_3 over a giant range. Sci Rep 2013;3:2458. https://doi.org/10.1038/srep02458.

[28] Azuma M, Chen WT, Seki H, Czapski M, Olga S, Oka K, et al. Colossal negative thermal expansion in $BiNiO_3$ induced by intermetallic charge transfer. Nat Commun 2011;2:347. https://doi.org/10.1038/ncomms1361.

[29] Takenaka K, Inoue N, Mizuno Y, Okamoto Y, Katayama N, Sakai Y, et al. Extended operating temperature window of giant negative thermal expansion in Sn-doped Ca_2RuO_4. Appl Phys Lett 2018;113(7):071902. https://doi.org/10.1063/1.5046463.

[30] Takenaka K, Okamoto Y, Shinoda T, Katayama N, Sakai Y. Colossal negative thermal expansion in reduced layered ruthenate. Nat Commun 2017;8(1):14102. https://doi.org/10.1038/ncomms14102.

[31] Xu S, Hu YM, Liang Y, Shi CF, Su YL, Guo J, et al. Negative thermal expansion of Ca_2RuO_4 with oxygen vacancies. Chin Phys B 2020;29(8):086501. https://doi.org/10.1088/1674-1056/ab8a36.

[32] Hu L, Zhu YC, Fang YW, Fukuda M, Nishikubo T, Pan Z, et al. Origin and absence of giant negative thermal expansion in reduced and oxidized Ca_2RuO_4. Chem Mater 2021;33(19):7665–74. https://doi.org/10.1021/acs.chemmater.1c01619.

[33] Coates CS, Goodwin AL. How to quantify isotropic negative thermal expansion: magnitude, range, or both? Mater Horiz 2019;6(2):211–8. https://doi.org/10.1039/c8mh01065j.

[34] Attfield JP. Mechanisms and materials for NTE. Front Chem 2018;6:371–6. https://doi.org/10.3389/fchem.2018.00371.

[35] Takenaka K, Takagi H. Zero thermal expansion in a pure-form antiperovskite manganese nitride. Appl Phys Lett 2009;94(13):131904–6. https://doi.org/10.1063/1.3110046.

[36] Yamada I, Marukawa S, Murakami M, Mori S. "True" negative thermal expansion in Mn-doped $LaCu_3Fe_4O_{12}$ perovskite oxides. Appl Phys Lett 2014;105(23):231906. https://doi.org/10.1063/1.4903890.

[37] Takenaka K, Kano M, Kasugai R, Takada K, Eto K, Kadowaki Y, et al. Structural phase transition and negative thermal expansion in $Cu_{1.8}Zn_{0.2}V_{2-x}P_xO_7$ solid solutions. Appl Phys Express 2022;15(2):025504. https://doi.org/10.35848/1882-0786/ac4926.

[38] Wang H, Yang MJ, Chao MJ, Guo J, Gao QL, Jiao YJ, et al. Negative thermal expansion property of β-$Cu_2V_2O_7$. Solid State Ionics 2019;343:115086. https://doi.org/10.1016/j.ssi.2019.115086.

[39] Zhang N, Li L, Wu MY, Li YX, Feng DS, Liu CY, et al. Negative thermal expansion and electrical properties of α-$Cu_2V_2O_7$. J Eur Ceram Soc 2016;36(11):2761–6. https://doi.org/10.1016/j.jeurceramsoc.2016.04.030.

[40] Zhu YW, Chen R, Chen L, Chao MJ, Guo J, Gao QL, et al. Negative thermal expansion property of $Zn_2V_{1.7}P_{0.3}O_7$. Solid State Sci 2021;112(2):106515. https://doi.org/10.1016/j.solidstatesciences.2020.106515.

[41] Shi N, Sanson A, Gao QL, Sun Q, Ren Y, Huang QZ, et al. Strong Negative thermal expansion in a low-cost and facile oxide of $Cu_2P_2O_7$. J Am Chem Soc 2020;142(6):3088–93. https://doi.org/10.1021/jacs.9b12442.

[42] Long YW, Hayashi N, Saito T, Azuma M, Muranaka S, Shimakawa Y. Temperature-induced A-B intersite charge transfer in an A-site-ordered $LaCu_3Fe_4O_{12}$ perovskite. Nature 2009;458(7234):60–U3. https://doi.org/10.1038/nature07816.

[43] Calvo C. The crystal structure of α-$Mg_2P_2O_7$. Acta Crystallogr 1967;23(2):289–95. https://doi.org/10.1107/S0365110X67002610.

[44] Kadowaki Y, Kasugai R, Yokoyama Y, Katayama N, Okamoto Y, Takenaka K. Structural phase transition and giant negative thermal expansion in pyrophosphate $Zn_{2-x}Mg_xP_2O_7$. Appl Phys Lett 2021;119(20):201906. https://doi.org/10.1063/5.0073761.

[45] Sun Y, Wang C, Huang QZ, Guo YF, Chu LH, Arai M, et al. Neutron diffraction study of unusual phase separation in the antiperovskite nitride Mn_3ZnN. Inorg Chem 2012;51(13):7232–6. https://doi.org/10.1021/ic300978x.

[46] Qiao YQ, Song YZ, Lin K, Liu XZ, Franz A, Ren Y, et al. Negative thermal expansion in (Hf, Ti)Fe_2 induced by the ferromagnetic and antiferromagnetic phase coexistence. Inorg Chem 2019;58(9):5380–3. https://doi.org/10.1021/acs.inorgchem.8b03600.

[47] Baitahe R, Vittayakorn N. Phase formation and evolution of Cu: Zn partials in binary metal pyrophosphates $Cu_{2-x}Zn_xP_2O_7$; x approximate to 1. Thermochim Acta 2014;596:21–8. https://doi.org/10.1016/j.tca.2014.08.038.

[48] Dhaouadi H, Touati F. Synthesis and characterization of a series of cobalt-manganese pyrophosphate $Co_xMn_{2-x}P_2O_7$ (x=0, 0.25, 0.5, and 1) compounds. Mater Lett 2012;82:91–4. https://doi.org/10.1016/j.matlet.2012.05.042.

[49] Yuan HL, Wang CY, Gao QL, Ge XH, Sun H, Lapidus SH, et al. Structure and negative thermal expansion in $Zr_{0.3}Sc_{1.7}Mo_{2.7}V_{0.3}O_{12}$. Inorg Chem 2020;59(6):4090–5. https://doi.org/10.1021/acs.inorgchem.0c00126.